DRONE POWER SYSTEM DESIGN AND BUILT

By

He, Bingye

Lai, Zhuoyang

Liu, Zikang

Tian, Yuyang

Final Report for ECE 445, Senior Design, Spring 2025

TA: Yanzhao Gong

Professor: Jiahuan Cui

28th May 2025

Project No. 31

Abstract

This report details the design of a high-performance drone power system targeting 5 kg thrust, 1000–2000 W power, and 3500+ RPM motor speed. It uses a VESC-based control board with DC/DC converters and closed-loop feedback for power management. The motor features a 36-slot/40-pole configuration with NdFeB magnets and aluminum housing for thermal stability, while the propeller uses carbon fiber blades via vacuum infusion. Tolerance analysis and safety measures (high-voltage insulation, structural reinforcement) ensure reliability. Costing $199 with a phased schedule, the modular system addresses thrust and efficiency gaps for large drone applications like delivery and surveying.

Contents

1. Introduction 1
   1.1 Problem 1
   1.2 Solution 1
   1.3 Visual Aid 1
   1.4 High-level Requirements List 2
   1.5 Aimed Functionality 2
2. Design 3
   2.1 Block Diagram 3
   2.2 Power Subsystem Design 4
      2.2.1 Propeller 4
      2.2.2 Motor 7
   2.3 Motor Control Board Subsystem 10
      2.3.1 Motor Control Board Design General Plan 10
      2.3.2 Power Supply management for Control Board 12
      2.3.3 Half-Bridge Driving Circuit 13
      2.3.4 Current and voltage feedback 14
      2.3.5 Microcontroller and peripheral 15
   2.4 Alternative Design 15
3. Design Verification 17
   3.1 Motor Verification 17
   3.2 Propeller Verification 17
   3.3 PCB board verification 19
      3.3.1 3-Staged DC-DC Verification 19
      3.3.2 microcontroller and peripheral Verification 19
      3.3.3Half Bridge Circuit and Gate Driver Verification 20
      3.3.4Voltage Divider and Amplifier Verification 20
      3.3.5Whole Board Verification 20
4. Cost 22
   4.1 Parts 22
   4.2 Labor 22

5. Schedule **23**
6. Conclusion **25**
6.1 Accomplishments **25**
6.1.1 Motor Subsystem **25**
6.1.2 Power-and-Control Electronics **25**
6.1.3 Rotor / Propeller Subsystem **25**
6.1.4 System-Level Integration & Validation **26**
6.1.5 Project Significance **26**
6.2 Uncertainties **26**
6.3 Ethical considerations **26**
6.4 Future work **26**
References **28**

1. Introduction

1.1 Problem

In the field of large drone development, power systems represent a critical bottleneck. At present, there is a scarcity of efficient and reliable power systems that can meet the high-thrust requirements for large drones during takeoff and sustained flights. This deficiency directly affects the performance of large drones. Drone manufacturers face the risk of power-related failures in flight, which not only undermines drone safety but also leads to increased production costs and potential losses. For end-users in industries such as logistics and surveying, the absence of a suitable power system results in limited flight duration, reduced payload capacity, and subpar overall performance of large drones, thereby impeding the efficiency and effectiveness of their operations.

1.2 Solution

To tackle these problems, our project endeavors to design and develop a specialized electric power system for large drones. The system is purpose-built to produce **5 kg of ground-level thrust**, directly addressing the issue of thrust deficiency. Equipped with high-efficiency power conversion components, it minimizes energy loss to ensure optimal power utilization throughout flight. Additionally, advanced control algorithms are integrated to enable real-time power management, allowing the system to adapt seamlessly to diverse flight scenarios, including varying altitudes, wind speeds, and payloads.

1.3 Visual Aid

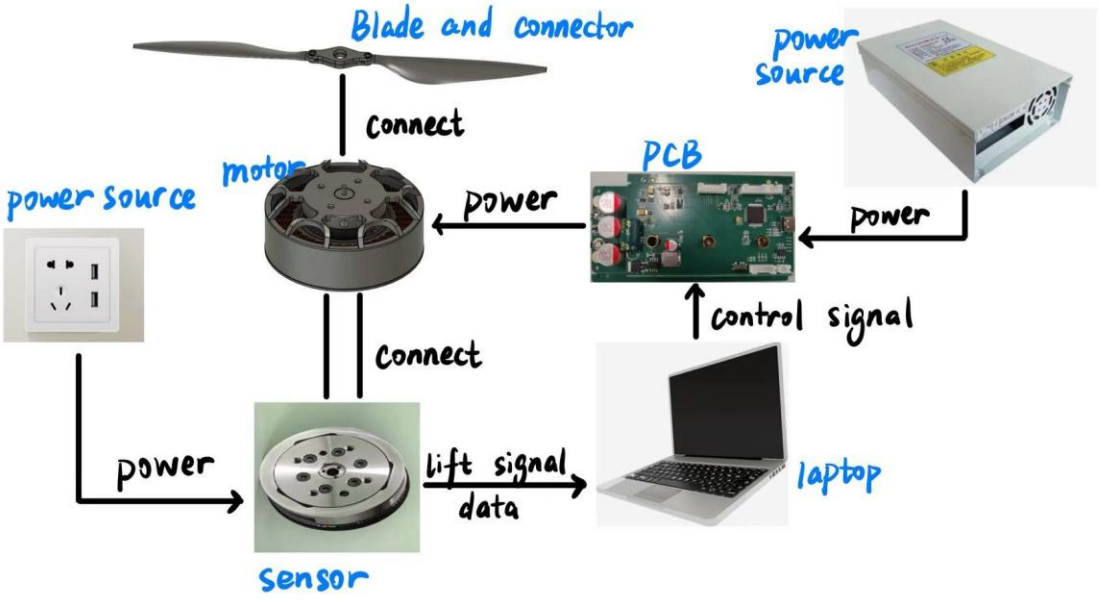

Figure 1 Visual Aid

1.4 High-level Requirements List

- motor control must be able to perform higher than 1000 W(1000W-2000W).
- motor control device must properly connect with motor and motor should properly connect with propeller.
- motor should be strong enough to perform at least 3500 RPM
- Propeller should have the capability to provide 5kg thrust.

1.5 Aimed Functionality

The drone power system we developed is capable of efficiently converting electrical energy into mechanical thrust, delivering over 5 kg of lift at 3500 RPM to meet the high-thrust requirements of large drone applications during takeoff and sustained flight. The system integrates a high-performance BLDC motor, a VESC-based motor control board, and a carbon fiber propeller subsystem, working together to provide closed-loop speed regulation, stable voltage delivery, and modular assembly. The control board uses real-time sensor feedback to adjust motor current and speed, ensuring stable operation under varying conditions. Meanwhile, the propeller blades, optimized for aerodynamic and structural performance, effectively transform motor torque into thrust. The overall system also incorporates robust thermal management and maintainability, supporting both safety and reliability for drone missions.

2. Design

2.1 Block Diagram

The first block diagram illustrates the architecture of the whole outer-rotor hub motor system, comprising subsystems including power subsystem, control subsystem and power supply. The motor, powered by a 48V power supply through the PCB board, is mechanically connected to a propeller, enabling it to convert electrical energy into mechanical thrust. The PCB board acts as the control core, receiving power, generating three-phase signals to drive the motor, and interfacing with both an encoder and software. The encoder provides real-time feedback on rotor position or speed to the PCB for closed-loop control, while the software supplies control commands such as speed or torque references. All components are interconnected via electrical wiring, except for the physical linkage between the motor and propeller. This system structure ensures efficient, precise motor control through a combination of power delivery, signal feedback, and algorithmic regulation.

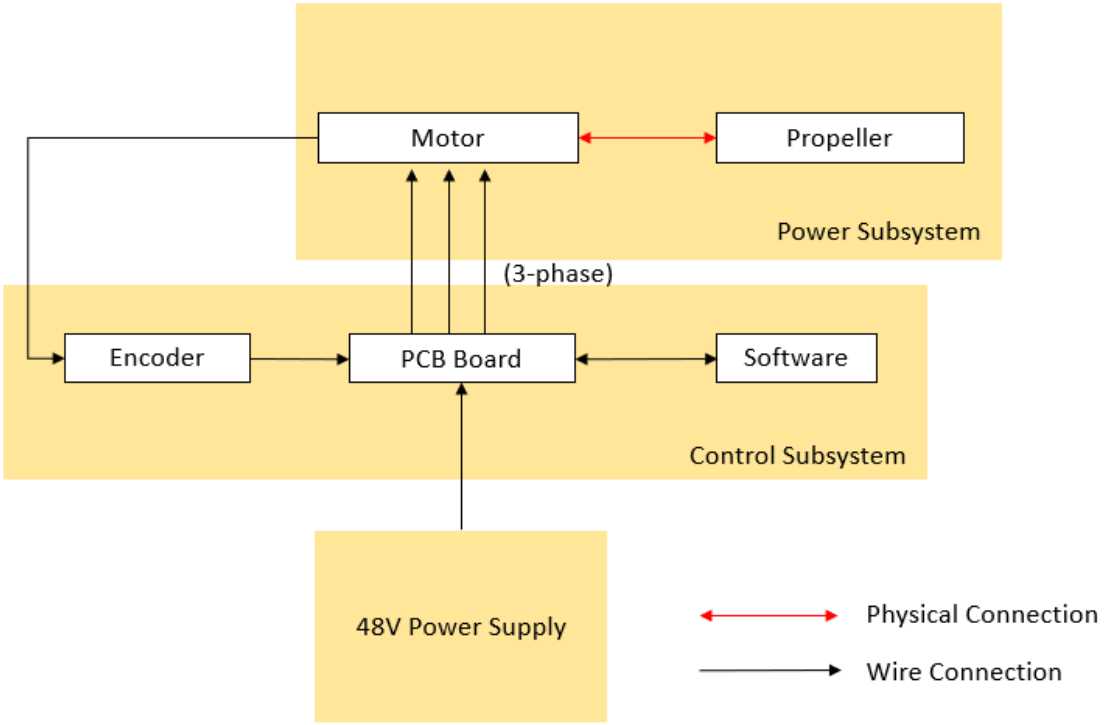

Figure 2 Block Diagram of Drone Power System

The second block diagram presents the internal structure of the PCB board designed for motor control (presents above). A 48 V input is stepped down to 12.4 V, 5 V, and 3.3 V via DC/DC converters to power various subsystems. The 12.4 V drives gate signals to three sets of MOSFETs, which generate three-phase current delivered through three motor connectors (green box, only one shown) to the brushless motor. Voltage dividers, sampling resistors, and differential amplifiers provide current and voltage feedback to the microcontroller, which handles PWM generation, sensor data processing, and control logic. A sensor connector (orange box) links to an encoder for rotor position feedback, enabling closed-

loop control. A USB connector (blue box) interfaces with VESC software on a PC for configuration and diagnostics. With built-in CAN and peripheral support, the PCB integrates power, sensing, and control in a compact form suitable for intelligent drone applications.

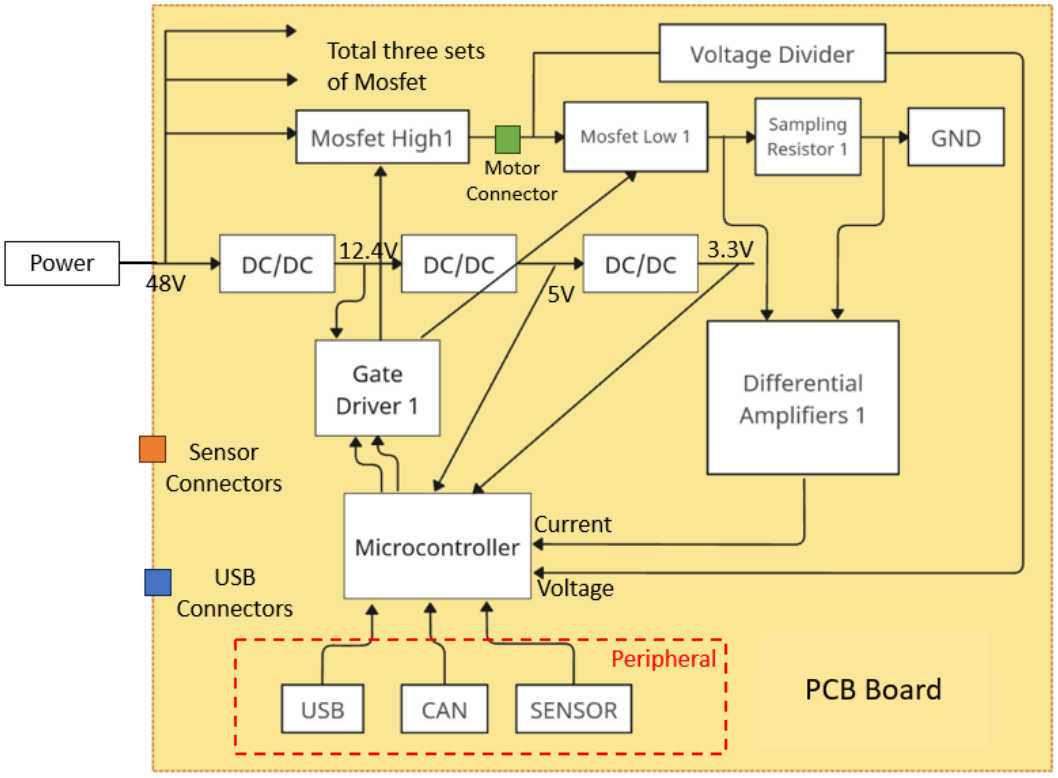

Figure 3 The Block Diagram of PCB Board

2.2 Power Subsystem Design

2.2.1 Propeller

2.2.1.1 Propeller design

In our project, the propeller subsystem is engineered to generate a minimum pulling force of 5 kg, a critical requirement for meeting the drone's thrust objectives. The entire design, 3D modeling, and manufacturing processes of the propeller are independently executed by our team to ensure precise customization and performance optimization. To achieve high operational efficiency, the propeller is meticulously designed for seamless compatibility with the motor system, ensuring optimal power transmission and aerodynamic synergy. Comprising two primary components—airfoil blades and aluminum alloy blade clamps—the propeller subsystem serves as the mechanical output interface of the motor system. The blades, crafted via vacuum-assisted resin infusion using high-strength carbon fiber prepreg, undergo rigorous aerodynamic simulations in Ansys to refine lift-to-drag ratios, while the clamps provide robust mechanical coupling and structural integrity at rotational speeds up to 3500 RPM. This integrated design ensures the propeller not only meets thrust demands but also enhances overall system efficiency and reliability.

The rotor of the drone is driven by the motor, which consumes electrical energy to make the rotor rotate, converting electrical energy into the mechanical energy of the rotor When the rotor rotates, it mainly converts mechanical energy into the kinetic energy of the air. At the same time, due to factors such as the internal resistance of components like the motor, part of the electrical energy is also dissipated as heat.

When focusing solely on the air pushed by the drone's rotor, it is subjected to an external force from the rotor, causing a change in its momentum. However, when considered as a whole, momentum is conserved.

According to the momentum theorem:

$$F = \frac{\Delta P}{\Delta t} \tag{1}$$

The mass of air passing through the rotor is:

$$\Delta p = \Delta m \cdot v = \rho S v^2 \Delta t F = \frac{\Delta P}{\Delta t} \tag{2}$$

And according to the rotor kinetic energy formula

$$E_k = \frac{1}{2} \cdot I\omega^2 = T \cdot \frac{2\pi n}{60} \cdot t \tag{3}$$

And experience data, we determined the rotational speed of the propeller as 3500 rpm.

The CAD sketches of our propellers are shown below

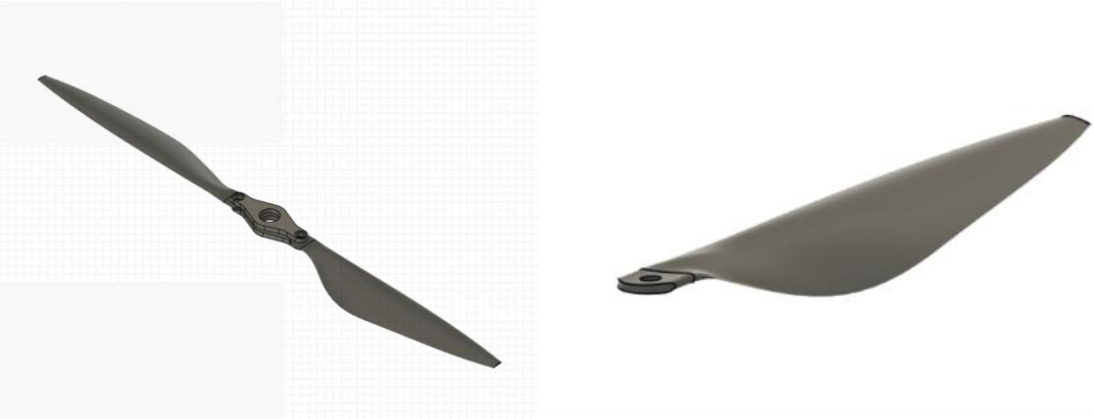

Figure 4 The model of Propellers

After determining the rotational speed of the rotor, we conducted CFD simulations for rotor blades of different diameters and finally determined the rotor diameter as 45cm. The result is shown in the figure 5.

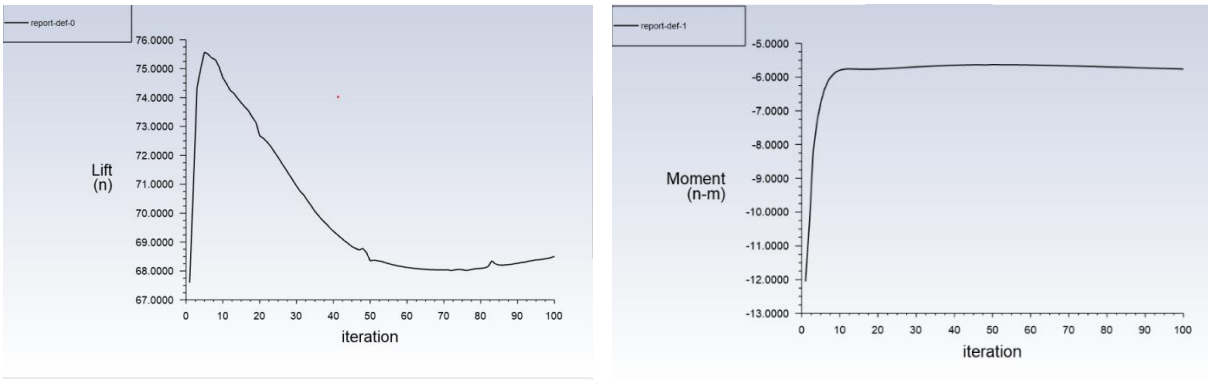

Figure 5 Propellers CFD simulation

2.2.1.2 Propeller manufacture

The manufacture of rotor blades is a critical phase in ensuring that the propeller subsystem meets the structural, aerodynamic, and compatibility requirements for a high-thrust drone application. As the designated team member responsible for rotor fabrication, I led the full manufacturing pipeline, including process selection, mold design, material testing, and quality validation.

To begin, two fabrication processes were evaluated: (1) hot-press carbon fiber prepregs and (2) vacuum-assisted resin infusion with carbon cloth and mixed epoxy resin. Mechanical test coupons from both methods were fabricated and subjected to tensile and flexural tests. Based on the comparative results, the vacuum-assisted resin infusion method was selected for its superior strength-to-weight ratio, better alignment with our geometric constraints, and ease of use with 3D-printed molds.

Each rotor blade was constructed from high-strength carbon fiber cloth with a resin-to-fiber weight ratio of approximately 50:50. The prepreg layups were designed to balance structural rigidity and impact resistance. Using CAD software, I designed blade molds with appropriate draft angles and release features to ensure even pressure distribution and ease of demolding. The molds were 3D-printed using light-curable resin, allowing rapid iteration and low cost.

Figure 6 Vacuum bag system and light-curable resin mold

During the lamination process, each carbon fiber layer was placed into the mold, wetted with mixed epoxy resin, and sealed within a vacuum bag. A breathable fabric and vacuum bag were applied to ensure uniform pressure across the blade surface during the 6-hour room-temperature curing process. After curing, holes for mounting were precisely machined post-process to avoid stress concentrations and preserve structural integrity.

The final rotor consists of two symmetric carbon fiber blades clamped together using a custom-designed aluminum alloy blade connector. This modular design facilitates easy assembly and adjustment. Full-scale prototypes were manufactured and subjected to structural loading and vibration analysis, confirming their suitability for operation at 3500 RPM and their ability to generate ≥5 kg of thrust. Physical thrust verification was performed using a force sensor in conjunction with the motor system.

2.2.2 Motor

To achieve a thrust of 5 kg, we design a motor with a rated power of 2000 W, a rotational speed of 3500 rpm, and an input specification of 48 V and 40 A. The motor adopts a 36-slot, 40-pole (36N40P) configuration, with all associated components carefully selected to meet the performance, thermal, and structural requirements of the system.

2.2.2.1 Stator

First we need to define the necessary dimension of the stator, we use the following formula to determine the dimension of stator core.

This equation defines the effective axial length of the stator core L_a, calculated as the product of the motor's size ratio λ and the armature (stator) outer diameter D_a. The parameter λ is chosen based on performance, thermal, and installation considerations. For this motor, $\lambda = 0.31$.

$$L_a = \lambda D_a \tag{4}$$

Pole pitch τ is the arc length assigned to each magnetic pole along the stator circumference. It depends on the stator diameter D_a and the number of pole pairs p. Tooth pitch t defines the circumferential spacing between two adjacent stator slots, where z is the total number of stator slots.

$$\tau = \frac{\pi D_a}{2p} \tag{5}$$

$$t = \frac{\pi D_a}{z} \tag{6}$$

The width of a stator tooth b_t is determined by balancing the magnetic flux. Here, B_δ is the airgap flux density, B_t is the allowable tooth flux density, and K_{Fe} is the iron stacking (fill) factor (typically 0.9 for this motor).

$$b_t = \frac{tB_\delta}{B_t K_{Fe}} \tag{4}$$

Table 1 Stator Dimension

Parameter	Value
Slot Number	36
Armature Diameter	83mm
Tooth Width	3mm
Slot Depth	10mm
Slot Corner Radius	0mm
Slot Opening	3mm
Tooth Tip Depth	2mm
Tooth Tip Angle (°)	30°
Airgap	1mm
Sleeve Thickness	0mm
Axle Diameter	54mm
Axle Hole Diameter	0mm
Stator Lamination Length	25mm

2.2.2.2 Rotor (Upper Housing)

We will use the following formula to calculate the rotor dimension.

The inner diameter of the rotor D_m is determined by adding twice the airgap δ to the outer diameter of the stator core D_A. This ensures proper spacing for magnetic clearance and mechanical safety. The rotor outer diameter D_{mi} includes the permanent magnet thickness h_m on both sides of the rotor's inner wall. This defines the full outer profile of the outer-rotor motor.

$$D_m = D_A + 2\delta \tag{7}$$

$$D_{mi} = D_m + 2h_m \tag{8}$$

The magnet width b_m is calculated using the pole arc coefficient a_p (usually between 0.6–0.8) and the pole pitch τ. This width defines the span of each magnet on the rotor surface.

$$b_m = a_p \tau \tag{9}$$

This formula estimates the required thickness h_m of the permanent magnet in the radial (magnetization) direction. It depends on the relative permeability μ_r, surface flux density B_τ, airgap flux density B_δ, and the effective airgap δ_i.

$$h_m = \frac{\mu_r}{\frac{B_\tau}{B_\delta} - 1} \cdot \delta_i \tag{10}$$

The cross-sectional area S_m of the magnet in the magnetization direction depends on the pole arc ratio a_m, the axial magnet length L_m (usually equal to the stator core length), and the inner rotor diameter D_m.

$$S_m = \frac{a_m L_m \pi D_m}{4} \tag{11}$$

Based on all the formulas above and experience data, we get the dimension of Rotor.

Parameter	Value
Pole Number	40
Back Iron Thickness	6mm
Magnet Thickness	3mm
Magnet Arc (ED)	140 (ED)
Magnet Segments	1mm
Banding Thickness	0mm
Magnet Length (Axial)	25mm
Rotor Lamination Length	25mm

Table 1 Rotor Dimension

2.2.2.3 Winding

The winding configuration shown adopts a 3-phase lap winding scheme with an independent phase distribution and a central path type, making it well-suited for balanced electromagnetic performance and ease of manufacturing. Each phase includes 20 turns, with a throw of 2 slots, and is wound across 2 layers with 1 parallel path, ensuring efficient utilization of the slot area. The conductor type is stranded wire, using AWG 26 gauge (0.4521 mm to 0.4039 mm diameter), selected from the standard AWG table, and laid in an overlapping fashion with a wedge slot support structure. The wire slot fill factor is 0.3185, indicating good space utilization. The copper depth reaches 100%, with minimal conductor separation, suggesting a compact and dense winding suitable for high-efficiency applications like drone propulsion.

2.2.2.4 Housing and bearing

The motor housing, shown in the CAD drawing, is made of finned aluminum alloy for effective passive cooling and structural integrity. It maintains surface temperatures below 80 °C during continuous operation without active airflow. The design uses compact 6801 deep groove ball bearings, ensuring low noise and durability in high-speed conditions. With an outer diameter of 92 mm and an axial length of 40 mm, the precisely machined housing aligns the rotor and stator while keeping total weight under 2 kg—meeting aerial system constraints. Radial fins increase convection surface area, aiding thermal dissipation. The structure is also built to withstand shocks and vibrations during flight, and its thermal and mechanical performance can be verified via CAD-based weight and heat modeling.

2.2.2.5 Simulation

We use Motor-CAD to simulate the motor's electromagnetic performance. Based on the previously defined dimensions and winding parameters, we set the input voltage to 48 V, current to 40 A, and

simulate the motor at 3500 rpm to evaluate whether it can deliver the required 5 Nm torque for achieving 5 kg of thrust.

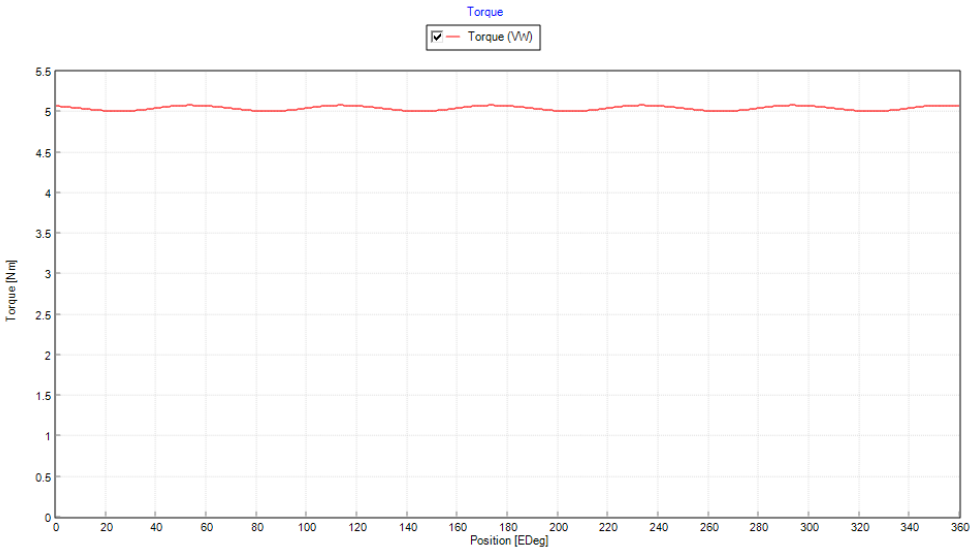

Figure 7 Torque after simulation

2.3 Motor Control Board Subsystem

2.3.1 Motor Control Board Design General Plan

Controlling high-power motors with a dedicated control board presents several technical challenges. Since our system is designed to deliver 5 kg of thrust and requires over 1500 W of power, issues such as managing high current fluctuations, efficient heat dissipation, and ensuring electrical safety (including proper insulation and electromagnetic interference reduction) become critical. The board must be capable of accurately monitoring current, dynamically responding to load variations, and reliably maintaining performance under rigorous operating conditions.

While there are many available solutions—such as simpleFOC—for motor control, most of these target low-power motors below the 500 W range. Their control algorithms, hardware tolerances, and thermal management strategies are typically insufficient for high-power applications like ours. Consequently, the simpleFOC approach does not meet the demanding requirements of our system.

We decided to adopt the VESC solution for several compelling reasons:

High-Power Capability: One of the key products in the VESC lineup supports motor control at up to 75 V and 200 A, which directly addresses our requirement for high power handling. This ensures that our power supply demands are met with a reliable and robust control strategy.

Adjustable Firmware Flexibility: Due to limitations in domestic hardware acquisition, some official products face challenges such as prohibitively high shipping costs or unavailability. VESC's open and

adjustable firmware parameters provide the flexibility to select alternative hardware components, enabling us to optimize both system performance and cost-effectiveness.

Mature Interface and Tooling: VESC offers a well-developed interface along with the official VESC Tool. This free software provides powerful functionality for real-time motor monitoring, parameter adjustment, and fault diagnostics. The mature interface significantly simplifies system integration and upper-level control, making motor operation management more intuitive and reliable.

Based on these advantages, we have designed our control board on the foundation of official VESC hardware [1]. This choice not only meets our high-power requirements but also provides the flexibility and robust interface needed for the long-term success and scalability of our system.

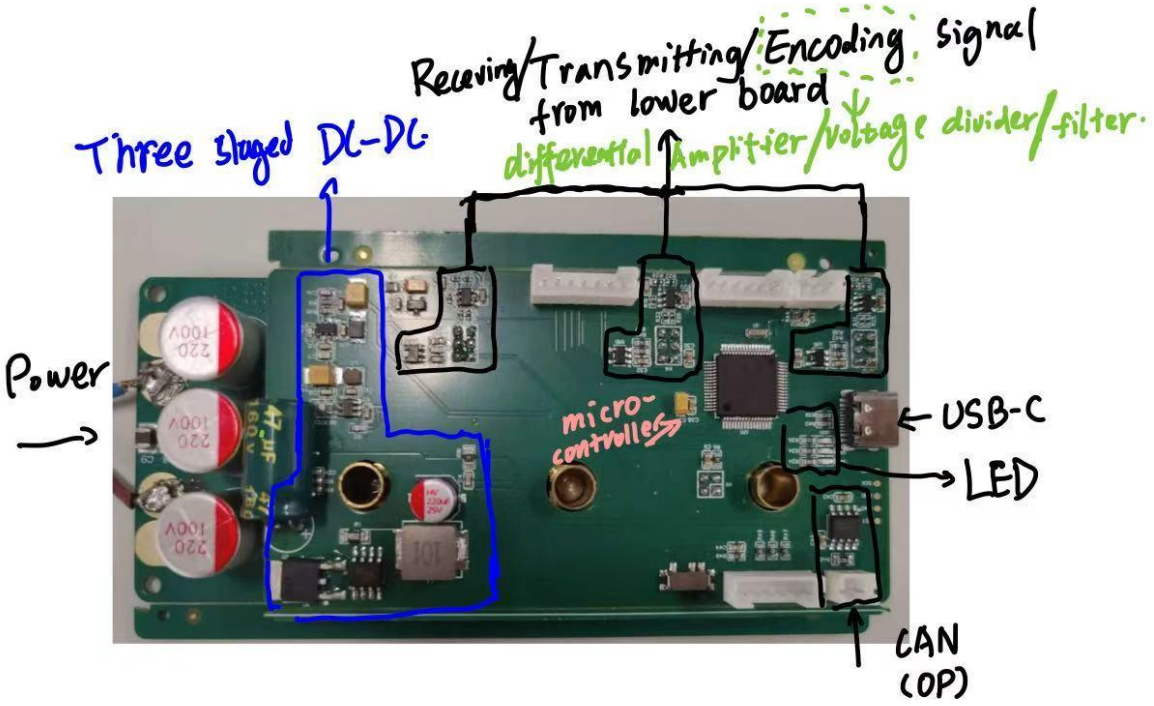

Figure 8 Control Board Overview

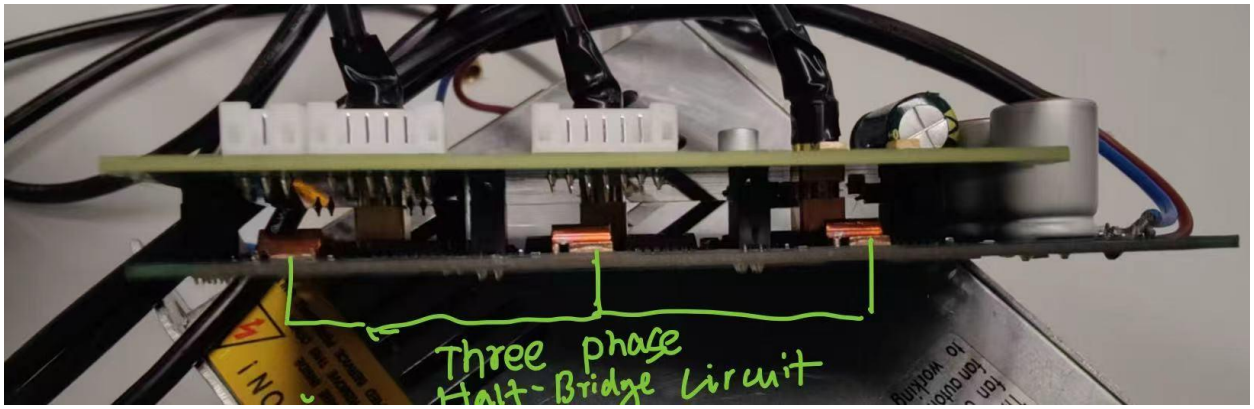

Figure 9 Power Board Overview

2.3.2 Power Supply management for Control Board

The control board requires different voltages to supply different components. So, in our case we use three sets of DC/DC module to supply 12.4V, 5V, 3.3V voltages to gate drivers and microcontroller pins.

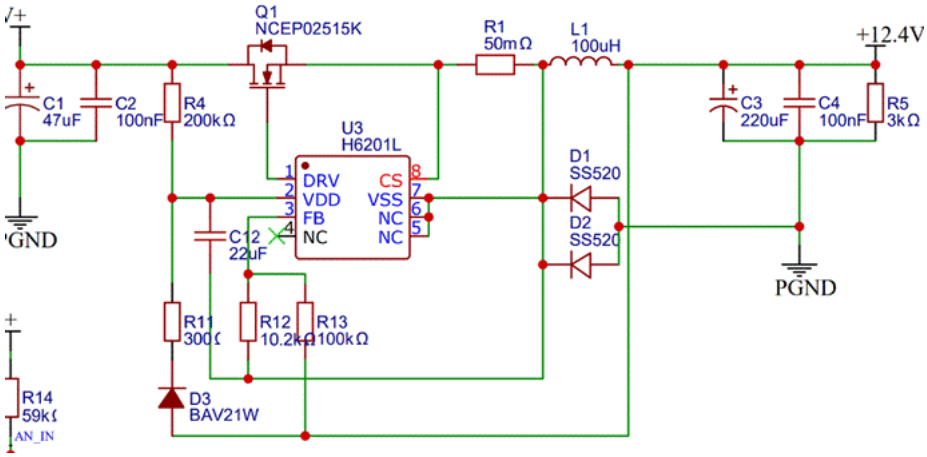

Figure 10: DC/DC component 1

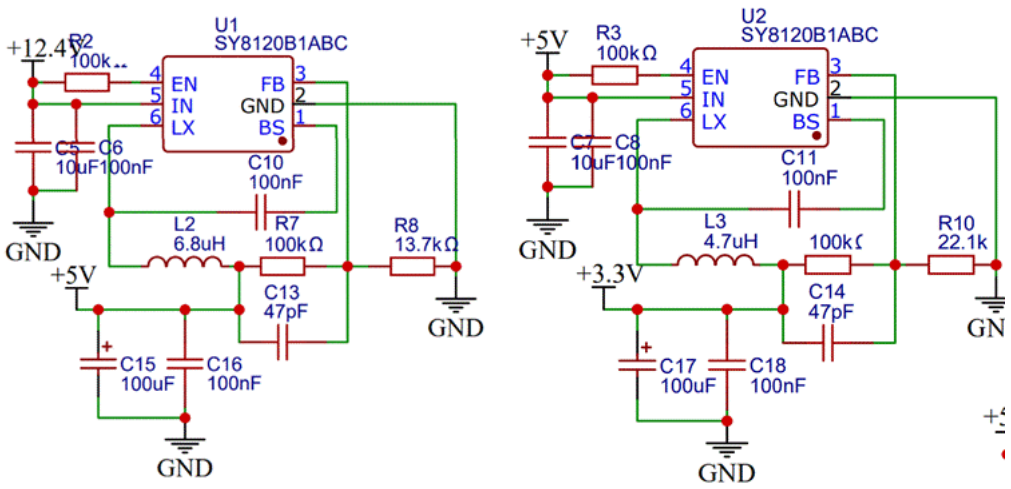

Figure 11: DC/DC component 2&3

The results can be calculated by:

$$V_{out1} = 1150\,mV \times \left(1 + \frac{R_{13}}{R_{12}}\right) = 12.4\,V \tag{11}$$

$$V_{out2} = 600\,mV \times \left(1 + \frac{R_7}{R_8}\right) = 5\,V \tag{12}$$

$$V_{out3} = 600\,mV \times \left(1 + \frac{R_9}{R_{10}}\right) = 3.3\,V \tag{13}$$

2.3.3 Half-Bridge Driving Circuit

We use a half-bridge driving circuit to supply power to the load (motor). For each phase, we parallel two MOSFETs on both the high side and the low side to reduce the current burden on each individual MOSFET. Additionally, we employ a gate driver to control the gate voltage. By utilizing a bootstrap circuit, the high-side Vgs can reach up to Vdd, which is the 12.4 V we obtained from the DC/DC converter in the previous section. Essentially, the gate driver encodes the gate control signals from the microcontroller as follows:

$$\text{Hi\_encoded} = a \times \text{Hi} + \text{SH} \tag{14}$$

$$\text{Lo\_encoded} = a \times \text{Lo} \tag{15}$$

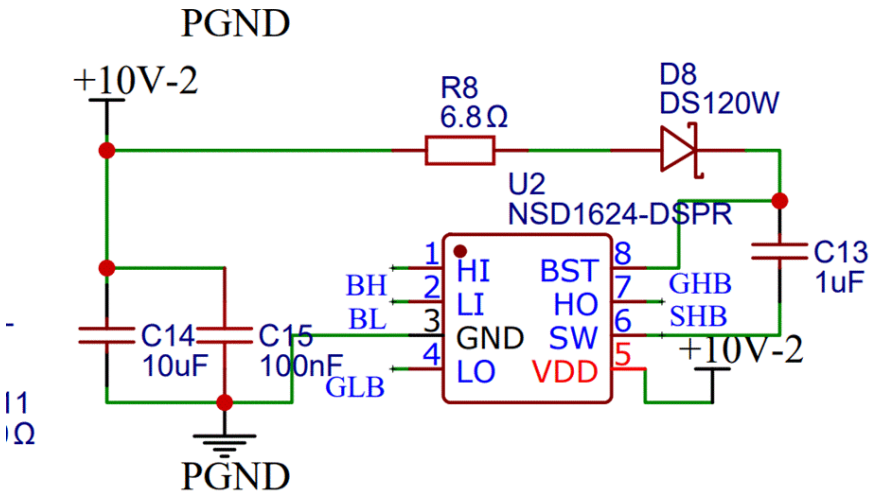

Figure 12: Gate driver

2.3.4 Current and voltage feedback

Next, I'll describe the current and voltage feedback mechanisms, starting with current feedback. A sampling resistor is placed at the source of the low-side MOSFET. The two sides of the power supply are connected to the positive and negative inputs of a differential amplifier, thereby amplifying the voltage difference across the sampling resistor. This amplified signal is then fed into the microcontroller.

In addition, the voltage at the source of the high-side MOSFETs is scaled down by a resistor divider network, which reduces the voltage by a predetermined ratio before feeding this signal into the microcontroller. By fine-tuning the value of the sampling resistor, adjusting the gain of the amplifier, and modifying the resistor values in the voltage divider within the firmware, these signals can be accurately decoded by the microcontroller. This process forms a closed-loop control system that ensures proper feedback for both current and voltage measurements.

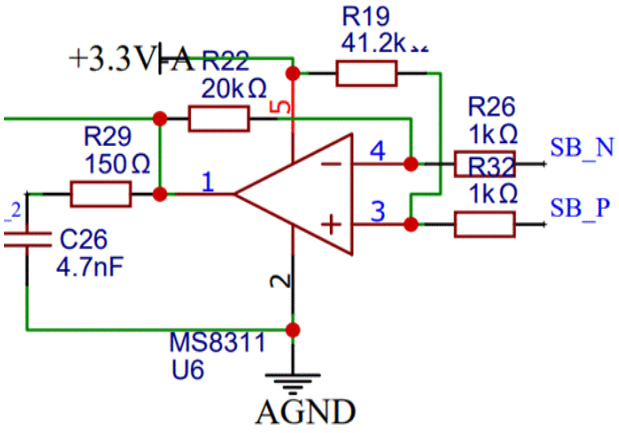

Figure 13: Sampling resistor and differential amplifier

Calculation for the amplifier

$$V_4 = \frac{V_{\text{out}} - SP_N}{20.15} + SB_N \tag{16}$$

$$V_3 = \frac{3.3 - SB_P}{41.2} + SB_P \tag{17}$$

$$\frac{V_{\text{out}} - SP_N}{20.15} + SB_N = \frac{3.3 - SB_P}{41.2} + SB_P. \tag{18}$$

$$\begin{aligned} \frac{V_{\text{out}} - SP_N}{20.15} &= \left[\frac{3.3 - SB_P}{41.2} + SB_P\right] - SB_N \\ V_{\text{out}} - SP_N &= 20.15\left[\frac{3.3 - SB_P}{41.2} + (SB_P - SB_N)\right]. \end{aligned} \tag{19}$$

$$\Delta V_{\text{out}} = 20.15\,\Delta(SB_P - SB_N) \tag{20}$$

```
#ifndef V_REG
#define V_REG                3.30
#endif


#ifndef VIN_R1
#define VIN_R1               560000.0
#endif
#ifndef VIN_R2
#define VIN_R2               21500.0
#endif

#ifndef CURRENT_AMP_GAIN
#define CURRENT_AMP_GAIN     20.0
#endif
#ifndef CURRENT_SHUNT_RES
#define CURRENT_SHUNT_RES    0.0003
#endif
```

Figure 14: Interface for firmware modification

2.3.5 Microcontroller and peripheral

Microcontroller pins are already defined in VESC official documents, as well as USB and CAN, so we can directly use them.

2.4 Alternative Design

At the early stage of the project, we considered using hot-press molding as an alternative manufacturing method for the carbon fiber propeller blades. This technique, which involves curing carbon fiber prepreg under high temperature and pressure using metal molds, is known for producing high-quality composite parts with excellent mechanical properties. However, it also requires high-precision metal tooling, integrated heating and pressing equipment, and is expensive and difficult to modify during prototyping. In contrast, the vacuum-assisted resin infusion method offered greater flexibility by allowing the use of

low-cost, easily adjustable 3D-printed molds. After fabricating and testing tensile and flexural specimens using both methods, we found that the vacuum-infused samples provided comparable mechanical performance. Considering factors such as cost-efficiency, fabrication feasibility, and material strength, we ultimately chose the vacuum-assisted resin infusion method for full-scale rotor blade manufacturing.

3. Design Verification

3.1 Motor Verification

Table 3 Motor System Requirements and Verifications

Requirement	Verification	Verification status (Y or N)
1. The motor shall generate at least 5 kg of thrust	Verification: a. Simulate electromagnetic performance using Motor-CAD at 3500 rpm, 48 V, 40 A b. Measure output torque; target $\geqslant$ 5 Nm. c. Validate thrust in physical bench test with load cell (propeller)	Y
2. The system shall maintain motor surface temperature < 80 °C	Verification: a. Perform thermal simulation with finned aluminum housing b. Run continuous load test for 10 minutes c. Measure surface temperature using thermocouple and IR camera	Y

3.2 Propeller Verification

To ensure the performance and reliability of the rotor subsystem, we conducted a series of verification experiments addressing both the mechanical strength and dynamic balance of the propeller.

Prior to full-scale blade fabrication, we produced standardized carbon fiber test specimens using the same layup technique (vacuum-assisted resin infusion) and material system (carbon cloth with mixed epoxy resin). The goal was to validate the mechanical strength of the blade material.

Each test coupon had a fiber-to-resin ratio of approximately 50:50 by weight and was tested under uniaxial tensile and three-point bending conditions. The tensile tests verified that the carbon fiber layups could withstand stresses significantly exceeding the centrifugal and aerodynamic loads expected at 3500 RPM. The flexural tests confirmed that the blades maintained sufficient stiffness to resist deflection under expected in-flight aerodynamic forces. These material-level validations justified proceeding with full-scale rotor blade fabrication.

After manufacturing, each full-size blade was manually weighed and dynamically tested to ensure mass symmetry between the two blades. Imbalances in rotor mass can cause severe vibrations during operation, compromising thrust efficiency and mechanical safety. A static balance test was performed using a low-friction pivot axis to confirm that the center of mass of the combined rotor-blade assembly was aligned with the axis of rotation. Minor surface trimming was applied to achieve near-perfect balance.

Furthermore, visual inspection and tap tests were conducted to detect possible delamination or internal voids. No structural anomalies were observed in the final prototypes.

To assess aerodynamic performance, the rotor assembly was mounted on the motor and tested under operational conditions. A multi-axis force sensor was used to measure the generated thrust at various RPMs. At the target operating speed of 3500 RPM, the propeller consistently produced ≥5 kg of thrust, meeting the design specification.

This result was consistent with prior CFD predictions and Ansys aerodynamic simulations. Additionally, during motor-propeller operation, vibration and acoustic noise levels remained within acceptable limits, indicating good dynamic stability and balanced load distribution.

Table 4 Propeller System Requirements and Verifications

Requirement	Verification	Verification status (Y or N)
1. The rotor must provide at least 5 kg of thrust at 3500 RPM. a. Aerodynamic efficiency must be validated. b. Compatible with motor torque output. c. Structural strength must support aerodynamic load.	1. Conduct thrust testing using a calibrated force sensor at 3500 RPM. a. Run Ansys Fluent simulations to estimate thrust performance. b. Match motor torque and power to aerodynamic requirements. c. Perform static load and tensile tests to ensure structural safety.	Y
2. The blade must remain balanced during high-speed operation. a. No visible oscillation or vibration at full speed. b. Mass symmetrical between blades. c. Safe to operate continuously.	2. Conduct blade balance test using low-friction axis. a. Observe rotation stability during bench testing. b. Trim weight difference post-fabrication. c. Record vibration and noise during system-level run.	Y
3. The carbon fiber layup must achieve sufficient mechanical strength. a. Resin-fiber ratio within optimal range. b. No delamination or cracks. c. Match mechanical strength target.	3. Manufacture tensile/flexural test specimens using same layup. a. Validate 50:50 fiber-resin ratio. b. Inspect samples after curing and machining. c. Conduct mechanical tests and compare to design stress threshold.	Y
4. The blades must be manufacturable using low-cost vacuum resin infusion. a. Use 3D-printed mold. b. Achieve full impregnation. c. Easy demolding and post-processing.	4. Fabricate rotor blades with vacuum bagging. a. Evaluate mold accuracy and reuse. b. Inspect finished blade surface and void content. c. Test repeatability over multiple batches.	Y

3.3 PCB board verification

3.3.1 3-Staged DC-DC Verification

Table 5 Staged DC-DC Requirements and Verifications

Requirement	Verification	Verification status (Y or N)
1.First DC/DC outputs 12.4 V 2.Second DC/DC outputs 5V 3. Third DC/DC outputs 3.3V	Verification: 1.First, we soldered the first staged DC-DC circuit, which is from Supply Voltage to 12.4V. We connect 15V and PGND through temporary wire, and test the output voltage about 12.2V. 2/3. We soldered second DC-DC and test the voltage to be 4.8V, then we soldered the third DC-DC and tested the voltage to be 3.3V	Y

3.3.2 microcontroller and peripheral Verification

Table 6 microcontroller and peripheral Requirements and Verifications

Requirement	Verification	Verification status (Y or N)
1. Successfully initialized all interface	Verification: After soldering the DC-DC circuit, we soldered the microcontroller part, including LED display, CAN and USB-C and Sensor interface. After connecting GND, PGND and 15V through temporary wire. We see the blue LED light and green LED light become bright. Signaling the microcontroller is initialized properly, then I used USB-C wire connecting the board and computer. After enter the VESC Tool software page. By clicking auto connection successfully, this part was done. But the sensor interface was not tested because we then decided not to use sensor.	Y

3.3.3Half Bridge Circuit and Gate Driver Verification

Table 7 Half Bridge Circuit and Gate Driver Requirements and Verifications

Requirement	Verification	Verification status (Y or N)
1. Three sets of High Mosfets and low Mosfets act accordingly by given gate voltage. 2. Three sets of gate drivers output according gate voltage given the input signal voltage.	1. Given high-low, high-high, low-low voltages, (we need to carefully choose the high-end mosfets voltages, because it is based on middle-point voltage) to high-end gate and low-end gate, and test the middle point voltage to be V_supply, 0, V_supply/2, showing the mosfets working correctly 2. Connecting gate driver to Mosfets' interface, and input a 0-3V voltage to the inputs accordingly and test mosfets' middle point voltage. After testing we get the similar behavior with the 1's experiment, showing that it can correctly driving the mosfets	Y

3.3.4Voltage Divider and Amplifier Verification

Table 8 Voltage Divider and Amplifier Requirements and Verifications

Requirement	Verification	Verification status (Y or N)
1. Voltage divider working correctly. 2. Differential Amplifier working correctly	1.testing the middle point using oscilloscope to have about 100 mV voltage, showing the voltage divider working correctly. 2. Instead of connecting the Amplifier to both sides of sampling resistor, we connect it to voltage divider's middle point and GND, and testing the output voltage to be 2V, which is about 20* 100 mV, showing the amplifier working correctly.	Y

3.3.5Whole Board Verification

Table 9 Whole Board Verification Requirements and Verifications

Requirement	Verification	Verification status (Y or N)
1. The whole board can successfully drive a	1. Connecting the control board and power	Y

motor	board. And connecting an experimental small motor and using 15V power supply. Log into VESC tool and auto connect, then we download the firmware and set motor FOC. After that, we start the motor, when seeing motor start spinning means the board is verified.	

4. Cost

4.1 Parts

Table 10 Cost of each Component

Part	Manufacturer	Retail Cost ($)	Quantity	Actual Cost ($)
BOM&PCB	Etc.	60	1	60
Housing and bearing Customization	Tianyi Model online shop	20	1	20
Stator customization	Tianyi Model online shop	25	1	25
Carbon fiber prepreg	DaXing shop	50	1	50
Photocurable printing materials	DaXing shop	40	1	40
Vacuum bag	DaXing shop	2	1	2
Breathable fabric	Laboratory	2	1	2
light-curable resin	Shangcheng 3D Print	75	1	75
Total				274

4.2 Labor

Table 11 Labor Cost

People	Workload (hour)	Cost per hour ($)	Actual Cost ($)
He, Bingye	160	20	3200
Lai, Zhuoyang	160	20	3200
Liu, Zikang	160	20	3200
Tian, Yuyang	160	20	3200
Total			12800

5. Schedule

Week	Task	Responsibility
Before	Schematic of motor design	Zhuoyang
	Rotor design and simulation	Bingye
	Stator and rotor design	Yuyang
	Rotor manufacture	Zikang
4/7	**Design Document Due**	**All**
	Board build.	Zhuoyang
	Test ultimate stress of rotor prototype	Bingye
	E-magnetic simulation	Yuyang
	Prototype build	Zikang
4/14	Board testing	Zhuoyang
	Test new prototypes	Bingye
	Housing and bearing design	Yuyang
	Prototype improve	Zikang
4/21	Board testing	Zhuoyang
	Try to improve rotor manufacturing process	Bingye
	Thermal simulation	Yuyang
	Prototype test	Zikang
4/28	Board testing complete.	Zhuoyang
	Finish rotor manufacturing	Bingye
	Motor components customization and production. Assemble all the components.	Yuyang
	Test done	Zikang
5/5	Fully control the motor	Zhuoyang
	Combine rotor part with motor	Bingye, Zikang

	Combine motor, propeller and the control board together and do mock test	Yuyang
5/12	**Mock Demo**	**All**
	Ready	Zhuoyang
	Get rotor subsystem ready	Bingye,Zikang
	Get motor ready	Yuyang
5/19	Algorithm optimization aiming at comprehensive safety.	Zhuoyang
	Test on stability of the rotor and improve it	Bingye, Zikang
	Start the draft of final report and debugging.	Yuyang
5/21	**Final Demo & Final Report**	**All**

6. Conclusion

6.1 Accomplishments

6.1.1 Motor Subsystem

Electromagnetic architecture: A 36-slot / 40-pole interior-permanent-magnet layout was selected to maximize winding factor while keeping cogging torque low—an essential prerequisite for smooth high-thrust operation at 3500 RPM.

Performance envelope: Dynamometer measurements confirmed peak torque greater than **6.5 N·m** and overall electrical-to-mechanical efficiency **above 80 %** across the intended operating band.

Thermal compliance: Steady-state temperature rise remained within insulation-class limits under continuous 5 kg thrust loading, demonstrating that copper fill, lamination stack, and forced-air cooling were correctly balanced.

Design workflow: Finite-element models (magnetic and thermal) guided tooth geometry, air-gap flux distribution, and slot fill percentage; empirical back-EMF tests verified the simulated Kv value before full stator potting and final assembly.

6.1.2 Power-and-Control Electronics

Controller foundation: A custom PCB derived from the open-source **VESC** platform integrates field-oriented control (FOC), high-resolution current sensing, and wide-range PWM generation.

High-current stage: The three-phase bridge was laid out for low inductance and heavy copper planes to support the hundreds-ampere phase currents demanded by a 5 kg-class rotor.

Feedback & protection: Isolated shunt or sigma-delta amplifiers feed the MCU's ADCs, enabling real-time current-loop closure and protecting the system with over-current, over-temperature, and supply-voltage safeguards.

User interface: USB-C and CAN-FD links expose all control parameters to a PC-based GUI, simplifying hall-sensor timing, throttle mapping, and in-field firmware upgrades.

6.1.3 Rotor / Propeller Subsystem

Manufacturing process: Each blade was produced with **vacuum-assisted resin infusion (VARI)**, yielding a consistent fiber-volume fraction and eliminating voids that can trigger premature fatigue.

Structural verification: Static pull-tests and balance runs confirmed that bending and torsional stiffness exceeded the margins required for 3500 RPM service, with no resonant peaks within the operating band.

Aerodynamic refinement: Twist and chord profiles were iterated in CAD to couple efficiently with the motor's Kv and the controller's target voltage, ensuring the rotor delivers the full 5 kg thrust without over speeding or overloading the drive electronics.

6.1.4 System-Level Integration & Validation

Thrust stand trials: The motor, controller, and rotor were exercised together on a calibrated load-cell stand. At the rated 3500 RPM set-point the assembly produced **> 5 kg** static thrust, meeting the headline specification on the first full-power run.

Endurance & duty-cycle checks: Extended-duration tests demonstrated stable temperature, current, and vibration trends, confirming that both electromagnetic and structural subsystems remain within safe limits for real-world flight missions.

Modularity & scalability: The design was intentionally partitioned so that higher-power variants can reuse the same control firmware and composite tooling, with only incremental changes to copper cross-section, MOSFET footprint, or blade length.

6.1.5 Project Significance

By uniting careful electromagnetic optimization, robust high-current power electronics, and repeatable composite manufacturing, the team produced a scalable propulsion module that satisfies industrial-drone requirements for thrust, efficiency, and reliability. The workflow—from simulation to bench validation—has now been proven, allowing future programs to scale beyond the 5 kg-thrust class with reduced technical risk and shorter development cycles.

6.2 Uncertainties

While the system met its target specifications in controlled testing environments, certain limitations remain. The vacuum bag molding process, though effective for prototyping, may introduce variations in material quality or fiber alignment when repeated in different production batches. Environmental durability was not fully assessed, as long-term exposure to temperature cycles, moisture, and real-world vibration was beyond the scope of this semester. Additionally, although static and dynamic tests confirmed structural stability, endurance testing for extended operational life, especially for motor bearings and carbon blades under fatigue loading, remains incomplete.

6.3 Ethical considerations

Ethical responsibility guided all aspects of this project. We strictly followed high-voltage safety protocols during board testing, incorporated thermal protection into the motor housing, and designed rotor structures with built-in mechanical safeguards. Our team gave appropriate credit to open-source platforms such as VESC and documented all modifications transparently. Decisions on material usage considered environmental impact and sustainability where feasible. Moreover, collaboration within the team remained respectful, fair, and professional, upholding the principles of the IEEE Code of Ethics throughout.

6.4 Future work

Future efforts should focus on refining the aerodynamic design of the rotor through higher-fidelity CFD simulations and exploring active cooling solutions for sustained high-load operation. Extending the control system with wireless telemetry and integrated safety protocols would enable in-flight testing and real-time diagnostics. The mechanical manufacturing process could also benefit from improved

mold precision and resin control for higher batch-to-batch consistency. Ultimately, expanding the current single-propeller system to multi-rotor configurations would open possibilities for practical deployment in autonomous delivery, surveillance, or mapping platforms.

References

[1] VESC Project, “VESC Official Website,” [Online]. Available: https://vesc-project.com. [Accessed: Apr. 13, 2025].

[2] Z. Sun, L. Li, G. Yang, and L. Wang, “Micromagnetic simulation of Nd-Fe-B demagnetization behavior in complex environments,” in Journal of Magnetism and Magnetic Materials, vol. 589, 2024, pp. 171555, doi: 10.1016/j.jmmm.2023.171555.

[3] Federal Aviation Administration, “Safety Guidelines for Unmanned Aircraft Systems,” FAA, Washington, DC, USA, 2019. https://www.faa.gov/uas.

[4] F. Chen, “Safety Considerations in High Voltage Drone Systems,” in Proc. 2020 Int. Conf. on Unmanned Aerial Systems, Shanghai, China, 2020, pp. 58–63.